PAPER

Check for updates

Enhancing the perovskite solar cell performance by the interface modification of Zn–Sn–O compound heterostructures

Ranjith Kumar Poobalan,[ad] Ramarajan Ramanathan, [ID] *[b] Chellakumar R.,[c] K. Ravichandran[c] and Michel Zinigrad[a]

Enhancing the performance of perovskite solar cells (PSCs) is one of the prime concerns of researchers worldwide. For PSC devices, it is essential to develop the individual layer efficiently and cost-effectively. This work emphasizes the possibility of employing Zn–Sn oxide-based composite materials as alternative electron transport layers (ETLs) in PSC devices. Pristine Zn_2SnO_4 (ZTO), composite ZTO–ZnO, and ZTO–SnO_2 heterostructure-based ETLs were prepared by a simple solid-state calcination technique and proposed as an alternative to the TiO_2 photoanode used in PSC devices. The power conversion efficiency of the designed PSCs was studied based on crystallinity, morphology, cross-section, roughness, contact angle, work function, and Raman analysis of the ETL material. TEM analysis confirms the phase pure ZTO and heterostructure formation as a function of material stoichiometry. Compared to the pristine ZTO, the ZTO–ZnO and ZTO–SnO_2 composites have enhanced PSC performance. The ZTO–SnO_2 composites exhibit better band matching and charge transfer behavior with the perovskite layer than the pristine ZTO and ZTO–ZnO composites. The ZTO–SnO_2 ETL-based PSC device displays a maximum efficiency of 15.9%, while ZTO–ZnO shows a maximum efficiency of 14.3%, which is more than 12.6% for the pristine ZTO. The results indicate that Zn_2SnO_4-based composites can be suitable for ETLs in PSC device fabrication.

1. Introduction

The need to transition from dependency on nonrenewable energy sources to renewable energy sources and to reduce global warming is a great concern.[1,2] There are several energy conversion processes (solar cells, hydropower, wind power, nuclear power, and fuel cells) and energy storage (battery and supercapacitor) technologies are explored for this concern.[1–5] Among them, the sun provides an enormous amount of energy (23 000 TW) in a year compared to other renewable energy resources.[1] By 2050, the world is estimated to need about 28 TW of electrical energy per year, which cannot be obtained from nonrenewable energy sources alone. In addition, the over-dependency on nonrenewable energy sources would lead to adverse effects like global warming.[1] We must use technologies to trap and convert solar energy to valuable energy to solve this energy crisis.[6] Although unlimited energy can be obtained from the sun, it requires efficient techniques to convert solar energy to electric power due to its low energy density. Photovoltaic technology has attained incredible consideration and has been utilized in various devices for the past few decades.[7] Recent research reports that by 2030 the photovoltaic market is estimated to be about US$5 billion.[8]

Perovskite solar cells (PSCs) are a cost-effective solar energy harvesting technology because of their facile way of fabrication and efficient solar power conversion compared to other technologies.[9] PSC technology is an effective way to develop a flexible energy source for wearable devices.[10] Additionally, from the material point of view, perovskite materials exhibit unique properties like high absorption coefficients across the visible spectrum.[9] The bandgap of the perovskite layer can be tuned by changing the material composition.[9] PSC fabrication advanced initially from 2013 to 2022 through materials engineering processes.[11] As a result, researchers had to work on materials engineering, and these efforts led to the development of a single junction PSC-certified efficiency of 25.5% under standard light illumination.[12] Additionally, PSCs have the advantage of fabricating multijunction and tandem structures with

[a] Materials Research Center, Department of Chemical Engineering, Ariel University, Ariel 4076414, Israel

[b] Department of Physics, Indian Institute of Science (IISc), Bangalore 560012, India. E-mail: rramarajan@iisc.ac.in

[c] Department of Nuclear Physics, University of Madras, Guindy Campus, Chennai – 600 025, India

[d] Department of Metallurgical Engineering and Materials Science (MEMS), IIT-Indore, Simrol-453552, India

Si-based solar cells and achieving higher conversion efficiency.[13] However, when it comes to commercialization, the stability of PSCs is a significant concern.[14] Researchers have been working on different ways to enhance the stability of PSCs.[15]

Recently, the interface modification of charge transport layers, the electron transport layer (ETL) and the hole transport layer (HTL), which play a pivotal role in PSC devices, has gained attention.[16] The interface surface between the charge transport and perovskite layers has been chiefly studied to enhance the device's performance, especially by modifying the charge carrier injection, extraction, recombination, and ion migration at the interfaces.[15] This is evident from several reports on improving the performance of PSC devices by modifying the ETL and HTLs.[17,18] TiO_2 is the more widely used ETL material in PSC devices.[14] However, the TiO_2 material is subjected to a post-deposition high temperature (~ 550 °C) heat treatment process to achieve the desired anatase phase formation and surface modification like a mesoporous structure.[19] This high-temperature preparation process is restricted for use in flexible devices.[19] Also, the over-dependence on TiO_2 for various applications has become a concern.[20] Therefore, exploring non-toxic alternate ETL materials with low-temperature processing is necessary to replace the traditional TiO_2 for PSC device fabrication.[15] Metal oxides such as ZnO, SnO_2, WO_3, $SrTiO_3$, and Zn_2SnO_4 were studied as alternatives to TiO_2 ETLs in PSCs.[21–25] Ashok et al. investigated Zn_2SnO_4 as an alternate ETL for improved power conversion efficiency (PCE) by modifying the surface features and obtained an efficiency of about 13.4%.[26] Abuhelaiqa et al. studied the effect of a SnO_2/TiO_2 bilayer ETL to enhance charge carrier injection from the perovskite layer. They reported a considerable enhancement in fill factor (FF) and open circuit voltage (V_{oc}) values along with decreased J–V hysteresis.[27] In recent years researchers also explored heterostructure-based composite materials for ETL application due to their improved charge transport properties.[28] Surface modification and band gap tuning processes have promoted charge transfer by minimizing the interfacial defects using heterostructures.[27] Also, the heterostructure-based ETL improves the recombination process and charge transport resistance and enhances the stability of the devices.[29] Sawanta et al. studied the charge carrier dynamics and transport behaviors of the perovskite layer and the top electrode by the interface engineering process to improve the device performance.[30] Snaith et al. reported that the first few hundred hours of device performance are mainly affected by an electrical shunting mechanism of PSCs.[31] The Zn–Sn-based composite heterostructure-based materials are also proposed for ETL application.[32] The composite heterostructure materials exhibit better band matching with the perovskite layer. In addition to moisture resistance and chemical stability, ZTO-based metal oxides effectively block the hole transport toward the photo-anode site and improve the device's performance.[26] Also, the Zn–Sn–O-based composite heterostructure has various potential applications.[32,33] Moreover, their excellent optoelectronic properties lead to enhanced charge transport properties.[26] This improvement

originates from heterostructure formation offering an effective charge transfer process at the perovskite–ETL interface.[32]

In this work, pristine ZTO, composite ZTO–ZnO, and ZTO–SnO_2 heterostructures were studied as electron transport materials in PSC devices. The PCE of the fabricated PSCs was evaluated using the developed ZTO-based ETLs. The performance of the fabricated PSC devices was investigated based on the crystallinity, surface, optical, and electrical transport properties of the ETL material. An accelerated aging test was carried out to identify the stability of the fabricated devices. A possible transport mechanism between the perovskite and ETL is proposed based on the obtained results. The heterostructure provides a low-cost path to manufacture highly efficient and stable PSC devices.

2. Experimental methods and characterization

2.1. Materials and methods

Pristine ZTO, composite ZTO–ZnO, and ZTO–SnO_2 heterostructures were synthesized by a simple solid-state calcination technique for ETLs in PSC devices. The detailed synthesis process has been reported in our earlier work.[34] In brief, the required amount of zinc and tin metallic powders were ball milled for 12 h in ethanol media to obtain homogenous composite powders. Subsequently, the obtained powders were annealed at 950 °C for 8 h in the presence of oxygen to obtain the final products.

2.2. Characterization

The structural and morphological properties of the prepared powder composites were characterized using a high-resolution transmission electron microscope (HR-TEM) operated at 300 kV (ThermoFisher® Titan™ Themis) and analyzed using Image J software. The powder samples were dispersed in absolute ethanol by ultrasonication and drop-cast on amorphous carbon-coated copper grids for TEM analysis. Raman spectroscopy analysis (LabRam HR Evolution, Horiba) was performed to study the obtained product's vibrational properties and chemical composition. The spectra were recorded using a 532 nm laser from 100 to 800 cm^{-1}. Before acquiring the spectra, calibration was performed using Si (520.7 cm^{-1}) as a reference. The cross-section and surface morphology of the developed composite films were examined using field-emission scanning electron microscopy (FESEM; Carl Zeiss Supra 40 VP) and Focussed-Ion-Beam (FIB; ThermoFisher® Helios G4-UX). The surface features and roughness of the films were characterized by atomic force microscopy (AFM; ANTON PARR) with probe radius >10 nm and scan area of 15×15 μm^2. A microscopic contact angle analyzer (OCA 50EC, Data Physics) assessed the wettability of the developed coatings in the static mode. The surface work function of the films was determined using a Kelvin Probe technique (Park NX20). All measurements were performed at room temperature. All measurements were performed at room temperature.

2.3. Fabrication of heterostructure ETL-based PSC devices

PSCs were developed with a normal (n–i–p) device structure on fluorine-doped tin oxide (FTO) coated glass substrates. Pristine ZTO, and composite ZTO–ZnO, ZTO–SnO$_2$ heterostructure materials were used as ETLs to fabricate three different PSC devices. The ETLs were prepared as follows: 2 g of each prepared material (ZTO, ZTO–ZnO, and ZTO–SnO$_2$) were individually mixed with 5 mL of ethanol (mixer), 0.2 mL of Triton X-100 (binder), and 0.5 mL of acetylacetone (solvent). The mixture was ground in an agate mortar pestle for one hour to obtain a homogeneous colloidal solution. Subsequently, the colloidal mixer was coated on FTO substrates (1.2 × 1.2 cm^2) by the doctor blade technique. Then the coated samples were annealed at 500 °C for 30 min in a muffle furnace and naturally cooled to room temperature. The thickness of these different ETLs is optimized around 300 nm. The post-annealed photoanodes were treated with ozone for 10 min. Then the photoanodes were transferred to a glove box (VTI-vacuum technology) to deposit the perovskite (methylammonium lead iodide, MAPI) and hole transport layer (HTL) (Spiro-MeOTAD) by the spin coating method. The MAPI and Spiro-MeOTAD precursor solutions were prepared following a previous report.[26] The thickness of the perovskite and HTL coatings was optimized via several trials. Finally, an Au electrode of thickness 120 nm was deposited by the thermal resistive evaporation method with a suitable mask. Three series of devices were fabricated and tested following similar fabrication procedures.

2.4. PSC testing

The power conversion efficiency (PCE, η%) of the different fabricated PSC devices was analyzed based on the photocurrent–voltage (J–V) characterization under AM1.5 illumination conditions using a Sol3A Class AAA Solar Simulator Measurements were conducted using a 150 W Xe lamp with a light intensity of 100 mW cm^{-2}. An Oriel SRC1000TC cell was used for calibration. Electrochemical impedance spectroscopy (EIS) analysis was performed using an electrochemical workstation (PARSTAT4000A AMETEK Scientific Instruments) at 10 mV in the frequency range of 0.1 Hz to 1 MHz. The photo-stability of the fabricated PSCs was investigated in indoor environments. To understand the degradation mechanism of the fabricated PSCs, the cells were stored under continuous illumination using a white LED lamp. The performance of photovoltaic devices was evaluated periodically by the protocol adopted at the International Summit on Organic Photovoltaic Stability (ISOS).[35]

3. Results and discussion

3.1. Transmission electron microscopy analysis

Fig. 1(a)–(c) show the HR-TEM micrographs of the synthesized ZTO, ZTO–ZnO, and ZTO–SnO$_2$ powders. It can be observed that the synthesized powder samples have polyhedron structures with average crystallite dimensions above 500 nm. The composites ZTO–SnO$_2$ and ZTO–ZnO have a relatively smaller crystallite size compared to ZTO. Due to the grain boundary

effect, this smaller crystallite size might contribute to the effective charge transfer process.[36] Selected area electron diffraction (SAED) pattern study was conducted to investigate the crystallinity and crystal structure of the systems. Fig. 1(d)–(f) display the obtained SAED patterns of ZTO, ZTO–ZnO, and ZTO–SnO$_2$ powder samples. The pattern confirms the polycrystalline and heterostructure formation of the samples, as reported in our earlier publication.[34] The obtained diffraction pattern of the pristine ZTO sample can be indexed as (111), (012), (113), and (222) planes of the cubic spinel structure of the Zn$_2$SnO$_4$ phase (JCPDS file No. 98-001-0595).[37] In the case of ZTO–ZnO composite heterostructures, in addition to the Zn$_2$SnO$_4$ phase, diffraction patterns conforming to the (011), (110), and (013) planes of the hexagonal ZnO phase (ICSD code: 98-005-2827) can be observed.[38] In the case of ZTO–SnO$_2$ heterostructures, besides the Zn$_2$SnO$_4$ phase diffraction patterns corresponding to the (011), (121), and (112) planes of the cubic SnO$_2$ phase (ICSD code: 98-006-5294)[39] can be perceived. Moreover, the ZTO sample exhibits a highly intense bright spot indicating the higher crystalline nature. In comparison, ZTO–ZnO and ZTO–SnO$_2$ samples exhibited bright rings, with multiple spots indicating the heterostructure formation.

Fig. 1(g) shows the HRTEM Bragg's pattern of the ZTO sample with the interlayer planer spacing of approximately 0.305, 0.261, and 0.241 nm conforming to the (111), (012), and (113) planes, respectively.[37] Similarly, the HRTEM Bragg's pattern (Fig. 1(h) and (i)) of the ZTO–ZnO and ZTO–SnO$_2$ heterostructure samples shows the presence of pristine ZTO planes along with the interplanar spacing of 0.247, 0.167 nm, and 0.243, 0.172 nm that can be attributed to the (110), and (013) planes of ZnO phase and (121), and (112) planes of SnO$_2$ phase, respectively. Thus, the obtained results confirm the heterostructure formation, and it also shows that the final product's phase depends on the precursors' stoichiometric ratio. The heterostructure formation is known to play an effective role in the charge transfer process of optoelectronic devices.[28] Samples with larger crystallite sizes lead to larger grains with a grain boundary.[40] A polycrystalline crystal structure has effective grain boundaries that control the mobility of charge carriers. The presence of more significant grain boundaries can affect the charge carrier transport properties due to the scattering process.[26] As a result, the stoichiometric ratios of the precursors can be adjusted to alter the charge transport properties of the samples.

3.2. Surface morphology analysis

Fig. 2(a)–(f) depict the FESEM surface morphology images and Focussed-Ion-Beam (FIB) cross-sectional images of fabricated PSC devices with a planar device structure with different ETLs. ETLs of all the devices exhibited a polyhedral surface morphology, which significantly impacts the performance device.[27] The FESEM images show a significant variation in surface morphologies based on their composition ratio (Fig. 2(a)–(c)). A sample with an excess of Zn content (ZTO–ZnO) has relatively bigger particles, whereas a Sn excess sample (ZTO–SnO$_2$) shows homogeneous particle formation with dense film formation.[34] In the
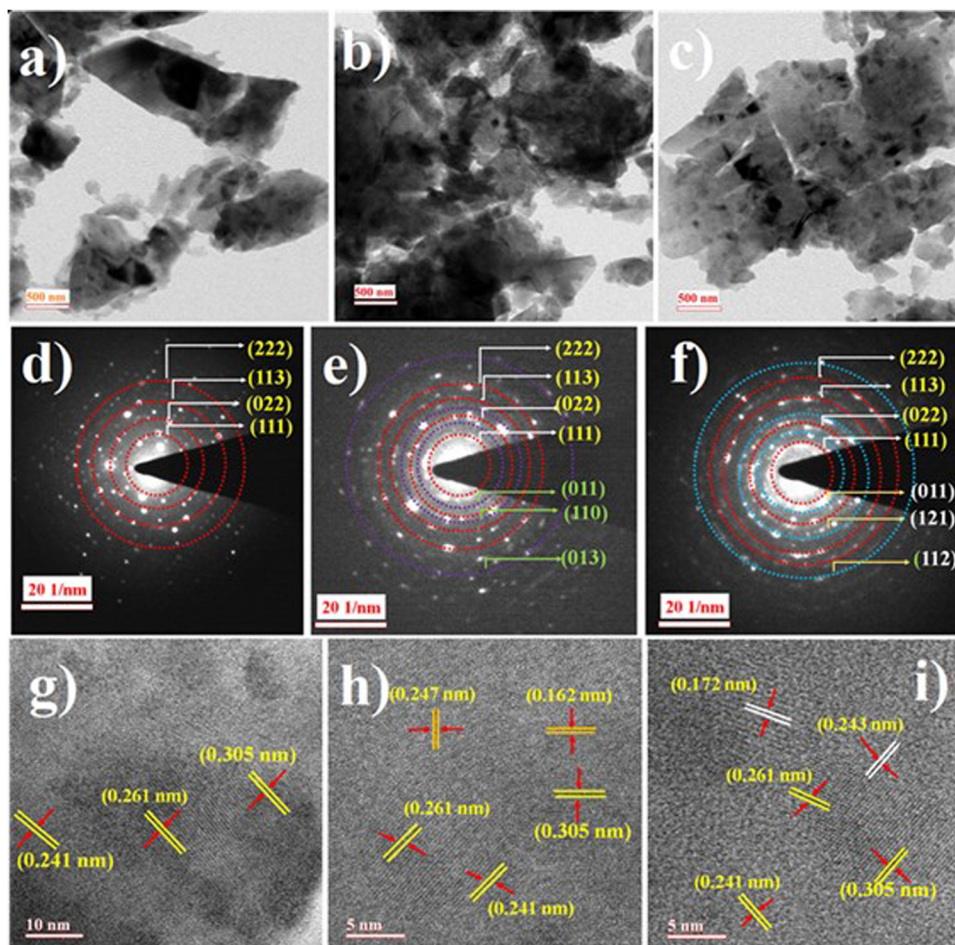
Fig. 1 Synthesized ZTO, ZTO–ZnO, and ZTO–SnO$_2$ samples topological features from the TEM (a)–(c), SAED (d)–(f), and HR-TEM (g)–(i) images indicating the heterostructure formation.

case of the pristine sample agglomerated particle formation leads to more surface roughness which can significantly affect the charge transfer process of the devices. It has been reported that the surface roughness of the thin film effectively controls the charge transfer process of the PSC device.[27,41] The cross-sectional FIB images exhibited significant variations in the cross-sectional film thickness due to the formation of different-sized particles.[29] It is also noted that the ZTO–SnO$_2$ film exhibited a relatively lower cross-sectional film thickness of 272 nm compared to other films. This high compactness of the film can facilitate the charge transfer process more effectively. The surface structure feature of ETLs strongly depends on Zn, Sn, and O elements in their stoichiometric ratio. However, the variation in the samples' stoichiometric ratio can create structural and surface defects. Generally, oxygen vacancies and/or ionic defects are the primary point defects in a metal oxide-based system.[42] These defects also play an important role in charge transport properties.[41]

3.3. AFM analysis

Fig. 2(d)–(f) illustrate the AFM images of the 3D surface topography of the pristine ZTO, ZTO–ZnO, and ZTO–SnO$_2$ composite

heterostructures coated on FTO substrates. The significant impact of the heterostructures on surface topography compared to pristine samples was observed. The surface topography changes from needle-like to granular structures for pristine ZTO to heterostructure samples. Hence, the sample with a needle-like topography has a relatively higher surface roughness than that with a granular structure.[43] Fig. 2(d)–(f) show the sample's root mean square (RMS) roughness evaluated from the AFM data. The ZTO–SnO$_2$ sample exhibited the lowest roughness value of about 13.47 nm. ZTO and ZTO–ZnO coatings showed higher roughness values of 28.46 and 19.82 nm, respectively, due to their needle-like surface structures. The RMS roughness and average roughness (R_{avg}) show similar variation for different ETL samples (Fig. 2(d)–(f)). These changes in the surface roughness might be due to the difference in the kinetics of grain growth during synthesis.[44,45] Grain growth increases due to a decrease in the grain boundary effect. During film formation, two or more larger grains might combine to form a needle-like structure, contributing to surface roughness.[45] The higher surface roughness of the films has a great impact on the charge transport process.[44] It is reported that carrier mobility decreases due to the increased surface roughness of the film.[44]
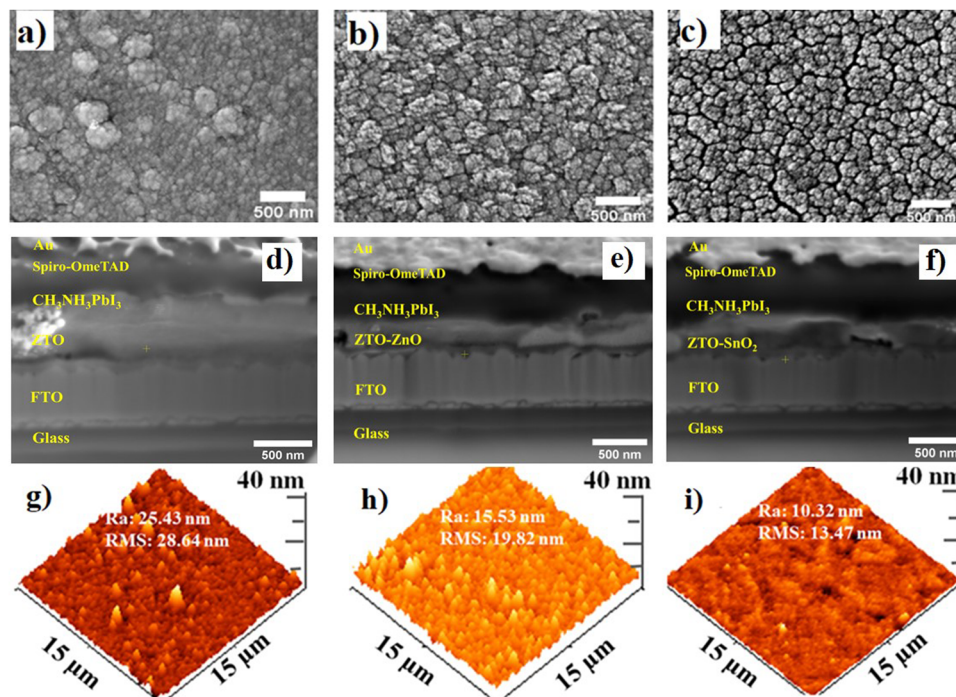
Fig. 2 (a)–(c) FESEM surface morphology images of fabricated ZTO, ZTO–ZnO, and ZTO–SnO$_2$ ETL-based perovskite solar cell devices, respectively. (d)–(f) FIB cross-sectional images of the ZTO, ZTO–ZnO, and ZTO–SnO$_2$ ETLs used in PSC devices. (g)–(i) AFM images of ZTO, ZTO–ZnO, and ZTO–SnO$_2$ coated on FTO substrates, respectively.

3.4. Contact angle measurement

Climate change and moisture in the atmosphere significantly affect the performance of PSC devices.[15] A contact angle measurement was carried out to examine the wettability of the coating and understand the stability of the fabricated devices upon exposure to water. Fig. 3(a)–(c) display the contact angles of water on ZTO, ZTO–ZnO, and ZTO–SnO$_2$ samples coated over the FTO substrate. The average contact angles of ZTO, ZTO–ZnO, and ZTO–SnO$_2$ coatings were 80.4, 89.1, and 96.0°, respectively. Generally, this high contact angle value indicates the strong hydrophobic behavior of the film, which means strong water-repelling behavior. However, this strong hydrophobic behavior of the ETL significantly influences the nucleation of the perovskite layer over the ETL.[46] Also, it is reported that the higher contact angle leads to an improved energy barrier for heterogeneous nucleation.[47] Hence, the charge transfer process at the ETL-perovskite interface is significantly affected by the higher

contact angle value.[47] Wen *et al.* reported that the surface-modified TiO$_2$-based ETL shows a relatively low contact angle compared to a pristine TiO$_2$-based device, which can facilitate the enhancement of the surface coverage of perovskite films.[48] These measured contact angle values indicated that the surface morphology of the films has a strong impact. Contradictingly it is also reported that the higher contact angle-based HTLs presented enhanced PSC device performance compared to the lower contact angle HTL sample. FESEM analysis showed that the ZTO–SnO$_2$ film is more compact compared to the pristine ZTO film. This highly compact nature of the heterostructure film may lead to a high contact angle value. A strong hydrophobic behavior of the film is more useful for preventing moisture penetration and controlling device degradation.[49] Hence, the strong hydrophobic features of the ZTO–ZnO and ZTO–SnO$_2$ heterostructures of the ETL can be more useful for inverted PSC structures to prevent moisture and improve the cell stability.
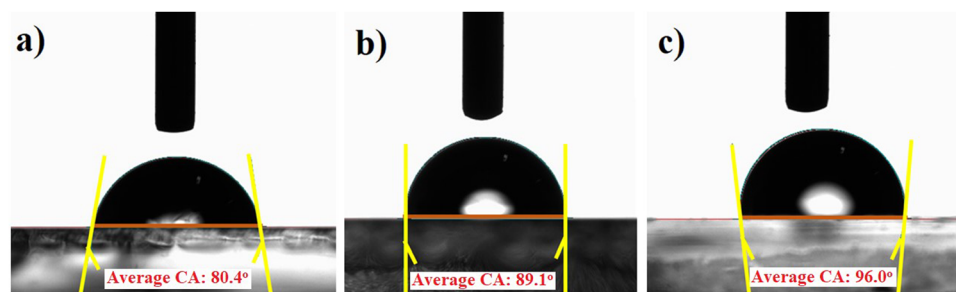

Fig. 3 Contact angle measurement of the synthesized (a) pristine ZTO, (b) ZTO–ZnO, and (c) ZTO–SnO$_2$ samples coated over FTO substrates.

3.5. Surface work function analysis

The surface work function (SWF) of the ETL plays an essential role in the charge transfer process in PSC devices.[50] The surface work function of a semiconductor is defined as the energy level difference between the Fermi level concerning the vacuum level ($\phi = E_{vac} - E_F$).[50] In ETL materials, the valence band maximum, and the conduction band minimum can be modified by altering the band gap of the material by different material engineering processes.[50] Also, the SWF can be altered due to variations in surface electronic properties.[51] The Kelvin probe technique was used for the SWF of the ETL measurement by estimating the contact potential difference (CPD) values scanned over the film surface at room temperature. The CPD value (work function) is recorded for the reference electrode. Stainless steel was used as the reference electrode (work function = 4.83 eV). The working principle of a Kelvin probe is similar to AFM analysis in conduct mode.[51] The variation of CPD of the film scanned over the 0.1 to 1 mm^2 area range was recorded, and the acquired values were plotted as a contour map, as shown in Fig. 4(a)–(c). The SWF of the film was measured using the following relation.[52]

$$\phi_{Film} = \phi_{Ref} - qV_{CPD}$$

where ϕ_{film} is the SWF of the film, ϕ_{Ref} is 4.83 eV, q is the electric charge and V_{CPD} is the average CVD values scanned over the film surface. The different ETLs show a significant variation in V_{CPD} values. The significant variation in V_{CPD} values due to variations in the surface behavior of the films includes surface morphology, roughness, surface charge transport properties, etc.[51] It is seen that the ZTO film exhibits more variation in V_{CPD} values compared to heterostructure-based devices. The estimated average SWF of the ZTO film is 5.14 eV, ZTO–ZnO is 5.10, and ZTO–SnO$_2$ is 5.05 eV (refer to Fig. 4(d)), and these values matched well with the previously reported values in the literature.[53–55] Variation in the SWF of films arises due to a significant shift of the Fermi level towards the vacuum level based on the heterostructure formation compared to the pristine film. Also, the SWF of the ETL with the perovskite layer and bottom electrode layer effectively controls the carrier injection/transfer process.[51–53] The obtained SWF values of the pristine and heterostructure-based ETL values suitable for the perovskite layer value (5.2 eV) and also the FTO electrode layer value (STD: 4.4 eV).[56,57] Hence, the SWF study indicates the possible applicability of synthesized ZTO, composite ZTO–ZnO, and ZTO–SnO$_2$ heterostructure samples as an ETL in a PSC device.

3.6. Raman analysis

The molecular vibrational modes and the surface functional group activity of the prepared pristine ZTO, composite ZTO–ZnO, and ZTO–SnO$_2$ heterostructure systems were investigated through the Raman spectroscopy technique. Fig. 5 shows the obtained Raman active vibrational signals from the synthesized samples, which confirms the presence of Zn$_2$SnO$_4$, ZnO, and SnO$_2$ phases. The intense peak at 669 cm^{-1} is related to the typical A$_{1g}$ symmetry of Zn$_2$SnO$_4$, which is the occurrence of the symmetric stretching of the Zn–O bonds in the ZnO$_4$ tetrahedra
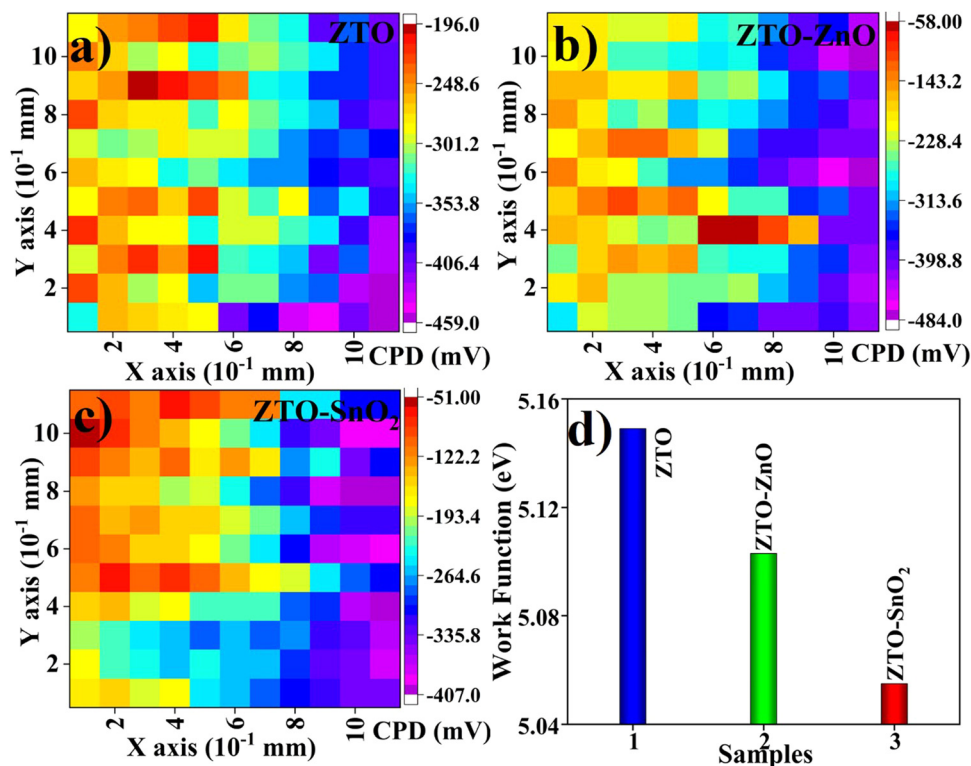

Fig. 4 Contact potential difference of (a) ZTO, (b) ZTO–ZnO, and (c) ZTO–SnO$_2$ samples coated over the FTO substrates scanned over an area of 1 × 1 mm^2. (d) The average surface work function of the ZTO, composite ZTO–ZnO, and ZTO–SnO$_2$ heterostructure samples.
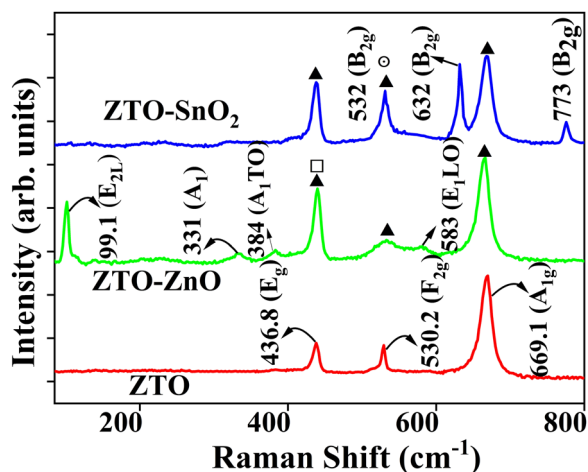
Fig. 5 Raman spectra of synthesized ZTO, ZTO–ZnO, and ZTO–SnO$_2$ heterostructure samples.

of the cubic spinel Zn$_2$SnO$_4$.[58] In addition, the other phonon modes at 530 cm^{-1} can be assigned to the F$_{2g}$ due to the symmetric bending of O atoms in the M–O bonds of the MO$_6$ octahedra (M = Zn or Sn).[59] The intense peak appearance at 438 cm^{-1} is analogous to the E$_g$ mode related to the silent mode of Zn$_2$SO$_4$, and this peak position is also associated with the ZnO phase Raman-active mode (E$_2$).[59,60] In ZnO and SnO$_2$ samples characteristic Raman active modes were absent in the pristine ZTO sample, thereby confirming the formation of a pure Zn$_2$SnO$_4$ phase. In contrast, ZTO–ZnO and ZTO–SnO$_2$ heterostructures exhibited the dominant Zn$_2$SnO$_4$ phase-related peaks and the ZnO and SnO$_2$ secondary phase peaks, respectively.

In the case of ZTO–ZnO, the vibrational mode detected near 99 cm^{-1} can be attributed to the vibrations of the zinc sublattice in ZnO.[59,60] The peaks at 330 cm^{-1} and 379 cm^{-1} are due to the second-order vibration mode (E$_{2L}$) and the A$_1$ transverse-

optical (TO) mode, respectively.[60] The peak at 332 cm^{-1} is analogous to multi-phonon scattering processes. In contrast, the E$_1$ longitudinal optical (LO) mode at 583 cm^{-1} can be attributed to oxygen defects such as vacancies or interstitials in ZnO.[60] ZTO–SnO$_2$ exhibits the characteristic Raman peaks at 632 cm^{-1} and 776 cm^{-1} that can be attributed to the A$_{1g}$ and B$_{2g}$ vibration modes, respectively.[37] The vibration occurs in the A$_{1g}$, B$_{1g}$, and B$_{2g}$ modes in the plane perpendicular to the c-axis, while in the E$_g$ mode in the direction of the c-axis.[37] The observed Raman peaks from the ZTO–ZnO and ZTO–SnO$_2$ samples indicate the heterostructure formation in the systems. Moreover, the spectrum of heterostructure-based samples shows a significant difference in the relative intensity and width of the vibrational peaks when compared with the pristine Zn$_2$SnO$_4$ sample. This confirms the heterostructure formation of the sample compared to a pristine ZTO sample.

4. Perovskite solar cell testing

The performance of the pristine ZTO, composite ZTO–ZnO, and ZTO–SnO$_2$ heterostructures as ETLs in PSCs was tested as an alternative to standard compact/mesoporous TiO$_2$ materials. Fig. 6 shows the schematic of the fabricated PSC devices with different ETLs and appropriate layer thickness. The standard planar device structure (FTO/(ZTO/ZTO–ZnO/ZTO–SnO$_2$)/MAPbI$_3$/spiro-MeOTAD/Au) has been followed for all the devices.[26] Band matching of each layer with the perovskite active layer is pictorially presented in Fig. 6(b). The J–V performances of the fabricated pristine ZTO, composite ZTO–ZnO, and ZTO–SnO$_2$ heterostructure ETL-based PSC devices were compared. The J–V characterization of all the devices under forward and reverse-biased conditions is shown in Fig. 6(c). The active light exposure area of the fabricated PSC devices is around 2 × 2 mm^2. The power of the incident light (100 mW cm^{-2}) is kept constant for all the devices.
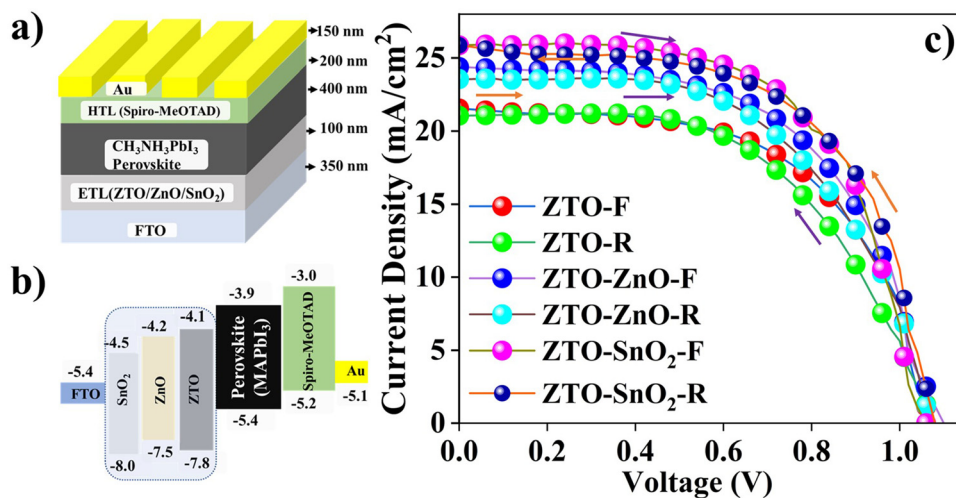

Fig. 6 (a) Schematic representation of the fabricated ZTO/ZTO–ZnO/ZTO–SnO$_2$ electron transport layers used in PSC devices with appropriate film thicknesses, (b) energy band diagram of the different ETL-based PSC device, and (c) J–V curves of the fabricated PSC device results compared with forward and reverse bias conditions.

4.1. Photocurrent–voltage (J–V) curve analysis

The power conversion efficiency (η) of pristine ZTO and ZTO–ZnO, ZTO–SnO$_2$ composite heterostructure-based PSC devices was examined using the photovoltaic parameters, open-circuit voltage (V_{oc}), short circuit current (J_{sc}), and fill factor (FF).[26] The respective photocurrent–voltage (J–V) plot is shown in Fig. 6(c) with two different biasing conditions (forward and reverse). The estimated V_{oc}, J_{sc}, and FF values are given in Table 1. Based on the obtained results of the studies on forward bias conditions, the pristine ZTO-based PSC device exhibits V_{oc} = 1.12 V, J_{sc} = 21.5 mA cm^{-2}, FF = 53.4, and η = 12.6%. In forward bias, it has been observed that the ZTO–ZnO composite-based device has V_{oc} = 1.10 V, J_{sc} = 24.3 mA cm^{-2}, FF = 53.6, and η = 14.3%. At the same time, the PSC device based on the ZTO–SnO$_2$ composite structure displays V_{oc} = 1.06 V, J_{sc} = 26.2 mA cm^{-2}, F = 57.4, and η = 15.9%. In the case of the reverse bias condition, all the devices show significant variation and follow a similar profile to the forward bias condition. Hence, the ZTO–SnO$_2$-based device shows a relatively improved photovoltaic behavior compared to ZTO–ZnO and pristine ZTO-based devices. An enhanced fill factor and current density were achieved due to a more surface-to-volume ratio of the dense and homogeneous surface morphology of the ZTO–SnO$_2$ sample compared to the surface morphology of the ZTO–ZnO sample.[34] The sheet-like surface morphology can promote effective charge transport at the interfaces between perovskite and ETL heterostructures.[28] The multiband structure of the heterostructure with other layers can be another cause for improved efficiency.[34] However, the devices' reverse biased J–V characteristic behavior showed relatively lower performance than the forward bias condition. These variations in the J–V curve indicate the hysteresis behavior of the device. Hysteresis can be due to the presence of several interfacial defects present in the device. The stability of a PSC device is easily affected by this hysteresis behavior.[61] The heterostructure interface decreases J–V hysteresis due to the reduction of interfacial charge accumulation and improves charge carrier extraction.[61] Also, it is reported that SnO$_2$/TiO$_2$-based heterostructure materials are introduced into the ETL for the stable

change transport process to decrease the hysteresis behavior.[27] Agresti et al. have studied the influence of light intensity on the current density with the n–i–p device structure.[62] They reported that the J_{sc} becomes higher in the presence of the graphene–SnO$_2$ heterostructure, which can reduce the hysteresis and enhance the charge extraction at the interface. The PSC device based on a standard TiO$_2$ ETL has a V_{oc} of 0.99 V, J_{sc} of 20.0 mA cm^{-2}, FF of 73.0, and η of 15.0%.[19] These values are relatively higher than our pristine ETL-based device since the pristine ETL-based device exhibits lower photovoltaic performance due to its low FF value. The low FF can facilitate the charge carrier recombination more effectively and decrease the current density.[62] The higher sheet resistance of the photoanode material is also one of the causes of yielding a very low photocurrent density. The fabricated ZTO-based device result is compared with other heterostructure-based devices reported in the literature and summarised in Table 1.[29,41,44,45,63–67]

4.2. Charge transport mechanism of PSC devices

The charge transport mechanism of the fabricated PSC devices can be explained based on the charge transfer process of the ETL with a perovskite layer and conducting electrode layer. The pristine ZTO ETL-based PSC device exhibits a charge transport mechanism similar to that of a TiO$_2$ ETL material-based PSC device.[68] In a PSC device, sunlight illumination leads to the excitation of the carriers in the perovskite (MAPbI$_3$) absorber from the HOMO to the LUMO level. During this process, these photo-excited charge carriers (exciton) separate in a fraction of a second. Subsequently, the separated charge carriers (electron/hole) are collected by the respective electrodes. Since, the power conversion efficiency of the PSC device strongly depends on the structural, surface morphology, and charge carrier transport process of the charge transport layers (ETL and HTL).[26] Charge transport layers must control the charge carrier injection/extraction, recombination, and diffusion process more effectively. The ETL/HTL are in contact with the perovskite layer. Therefore, suitable band matching of the ETL/HTL can lead to better performance. In the case of a composite heterostructure-based device, the charge transport mechanism is different from that of the pristine ZTO-based PSC device. In a pristine ZTO ETL-based device, the charge carrier transfer from perovskite to the ZTO ETL is based on the single charge transfer process. Fig. 7(a) and (d) shows the cross-section schematics of the ZTO ETL-based PSC device structure and the energy band structure with the charge transfer process of the device. Effective electron carrier transport occurs from the LUMO level of the perovskite into the ETL conduction band (E_C) during light illumination. Hence, the ETL charge transport properties effectively control the charge carrier collection of the photoanode. A pristine ZTO sample has relatively high charge transport resistance due to interfacial defects that affect carrier mobility.[28] Also, a large amount of generated charge carriers from the perovskite absorber is accumulated at the interface due to the low carrier transfer ability of a pristine ZTO-based ETL. Such accumulation of charge carriers at the interface can facilitate recombination processes leading to low device performance. The ZTO–ZnO

Table 1 Photovoltaic performance of pristine ZTO and composite ZTO–ZnO and ZTO–SnO$_2$ heterostructure-based PSC devices with other reported heterostructure-based PSC devices

| Samples	V_{oc} (mV)	J_{sc} (mA cm^{-2})	FF (%)	η (%)	Ref.
ZnO-F	1.12	21.1	53.4	12.6	Present work
ZnO–R	1.08	21.4	53.8	12.4	
ZnO–ZnO–F	1.10	24.3	53.6	14.3	
ZnO–ZnO–R	1.08	23.5	54.8	13.9	
ZnO–SnO$_2$–F	1.06	26.2	57.4	15.9	
ZnO–SnO$_2$–R	1.08	25.8	54.9	15.3	
TiO$_2$–SnO$_2$	1.04	23.2	66	15.9	29
SnO$_2$-TiO$_2$	0.97	21.7	71	14.9	44
SnO$_2$–ZnO	0.58	25.4	98.2	10.1	45
ZnO–SnO$_2$	1.15	21.74	76.4	19.1	41
ZnO–ZnS	1.12	24.1	76.6	20.7	63
a-WOx/SnO$_2$	1.11	22.9	80.15	20.44	64
SnO$_2$/CdS	1.03	23.08	72.2	17.1	65
Fe$_2$O$_3$@SnO$_2$	1.6	7.88	80.85	10.23	66
SnO$_2$/BaSnO$_3$	1.02	22.8	66.3	15.5	67
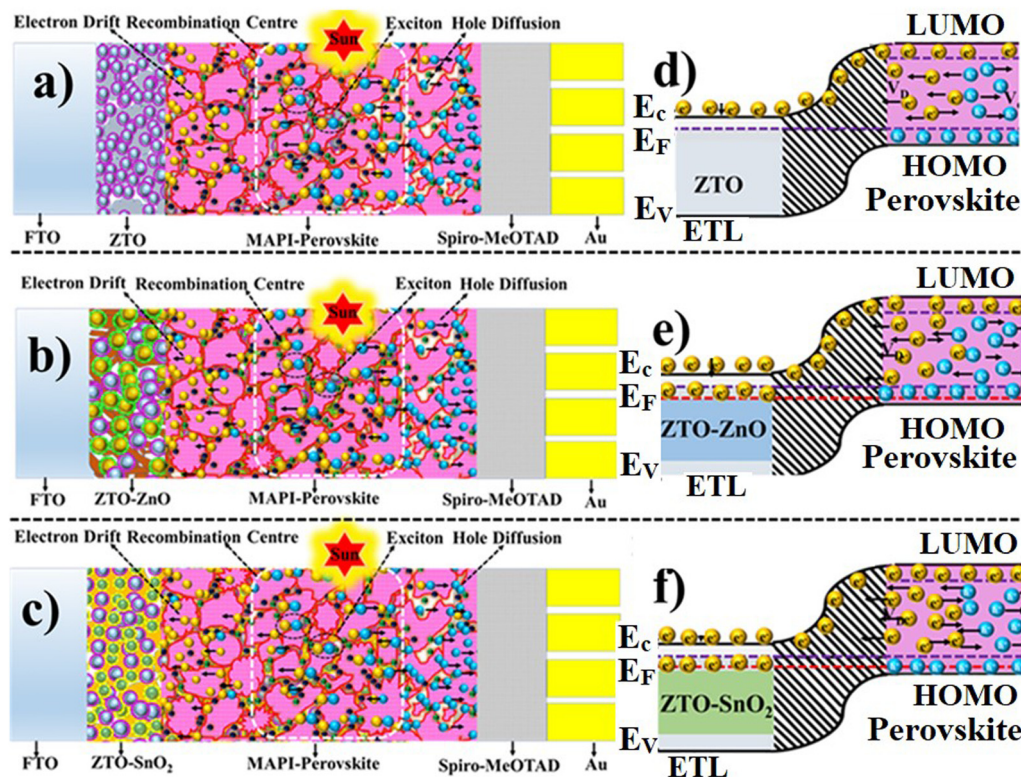
Fig. 7 Schematic representation of pristine ZTO (a) and (b), ZTO–ZnO (c) and (d), and ZTO–SnO$_2$ (e) and (f) heterostructure-based ETLs used in PSC device structures and with an appropriate energy band diagram with different ETLs.

and ZTO–SnO$_2$ composite heterostructure offers the multi-charge transfer process due to their multiband structure. Fig. 7(c)–(f) show the cross-section schematics of the ZTO–ZnO and ZTO–SnO$_2$ ETL-based PSC device and the corresponding energy band structure with the charge transfer process. In heterostructure-based devices, charge transport occurs in two ways; charge transfer *via* the main ZTO phase and second is through the secondary phase of ZnO/SnO$_2$.[29] For example, in the ZTO–SnO$_2$ heterostructure-based device, band matching occurs in two ways in the perovskite layer.[34] Band matching between the perovskite-ZTO and perovskite–SnO$_2$ phases offers two-way charge transfer processes. The multi-transfer process of this heterostructure effectively controls the charge carrier accumulation at the interface and hence regulates the recombination process.[34] Also, it can be noted that the ZTO–SnO$_2$ ETL-based PSC device exhibits better performance compared to the ZTO–ZnO-based device due to its sheet-like surface morphology.[34] Therefore, the surface modification of the ETL influences the transfer process more effectively.[34] Transferring the charges in dense surface structures is relatively more accessible than in in-homogeneous/agglomerated surface structures.

The mobility of charge carriers is affected by the agglomerated surface structure, whereas in dense surface structures, charge transfer occurs more effectively. Hence, the heterostructure-based device has an advantage over the pristine device due to its effective charge transfer process.

4.3. Study of electrochemical impedance spectroscopy (EIS)

The charge transfer mechanism in the pristine ZTO and ZTO–ZnO, ZTO–SnO$_2$ composite heterostructure-based PSC devices was investigated as a function of frequency using electrochemical impedance spectroscopy (EIS).[69] A data acquired from the EIS measurement was further investigated using EC-Lab software. In the EC-Lab software, we process the experimental data with the most suitable equivalent circuit data analysis.[69] An equivalent circuit is characterized based on the circuit elements like a capacitor, resistor, inductor, *etc.*[70] The deviation of these elements was further analyzed from the constant phase elements (Q) and electric double-layer capacitors (C_{dl}).[70] A constant phase element has a frequency-independent negative phase between current and voltage that interpolates between capacitors and resistors. Electric double-layer capacitors (C_{dl}) can be viewed as parallel circuits consisting of a large number of miniature capacitors with internal resistance.[70] Fig. 8(a) and (b) show the obtained Nyquist plots of the different ETLs, and the corresponding equivalent circuits. The high-frequency region of the real axis denotes the sheet resistance (R_s) between the photoanode and the perovskite interface. This low-frequency region denotes the diffusion resistance (R_1) at the interface between the counter electrode and perovskite. The constant phase elements (Q) further analyzed the charge transport and diffusion resistance behavior. The Nyquist plot shows that all the devices exhibit a single semicircle. The higher frequency region from 1 MHz to 1 kHz
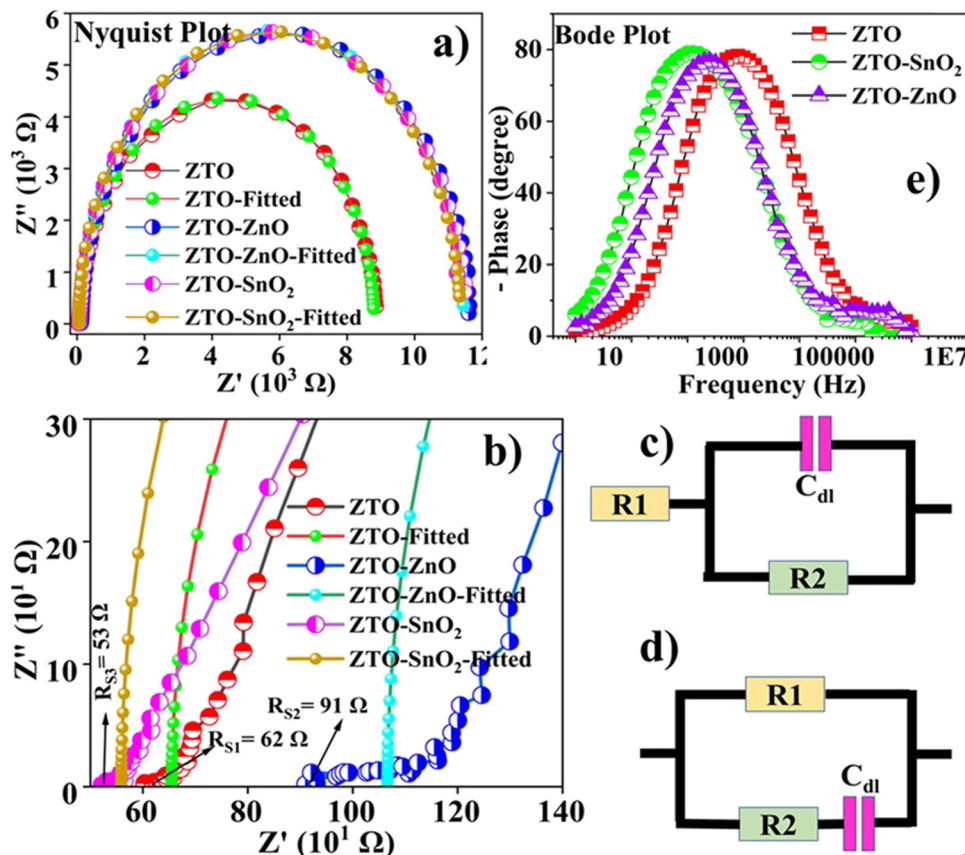
Fig. 8 (a) Electrochemical impedance spectra (Nyquist plot) of ZTO, ZTO–ZnO, and ZTO–SnO$_2$ ETL-based PSC devices, (b) extended view of the Nyquist plot in the higher frequency range, (c) and (d) the equivalent circuit used for the J–V curve analysis, and (e) Bode plot of the fabricated devices.

shows a relatively smaller semicircle indicating the sheet resistance (R_s) of the pristine and heterostructure-based photo-electrodes. The second larger semicircle in the lower frequency, from 1 kHz to 1 Hz, presents more charge transport resistance at the perovskite–photoelectrode interface. Injection and collection of charge carriers are affected by higher charge transport resistance.[71] However, no diffusion resistance is formed between the counter electrode and perovskite layer, indicating effective charge carrier collection. It is identified that the charge transport properties of the PSCs significantly changed with the heterostructure. The modified surface structure of the composite phase leads to a decrease in the charge transport resistance and diffusion resistance at the interface. The device fabricated with a heterostructure shows low sheet and charge transfer resistance, which might cause improved PCE compared to the pristine ZTO sample.[72]

The pristine ZTO ETL-based PSC device exhibits a much higher R_1 value of 8734 Ω, leading to a decline in carrier mobility. The ZTO-based device shows a high Q value which indicates a relatively low charge collection at the counter electrode. While the Q values of the heterostructure-based devices are lower, they exhibit improved charge carrier collection at the counter electrode.[34] However, we do not deny that the lower charge transport resistance identified from the second semicircle region facilitates more charge carrier

recombination, which is confirmed by lower Q values. The Bode plot provides an insight into the charge transport process more preciously.[34] Notably, the Bode plot provides the lifetime of charge carriers using the following relation (τ) = $1/2pf_{max}$, where f_{max} is the highest cut-off frequency.[34] Fig. 8(e) illustrates the Bode plots of the pristine ZTO and ZTO–ZnO, ZTO–SnO$_2$ composite heterostructure-based PSC devices. From the plot, it can be estimated that the highest cut-off frequency of ZTO is 794 Hz, ZTO–ZnO is 251 Hz, and ZTO–SnO$_2$ is 100 Hz. The determined lifetime of the charge carriers for the pristine ZTO, ZTO–ZnO, and ZTO–SnO$_2$ heterostructure ETL-based devices is 1.2 ms, 3.9 ms, and 10 ms, respectively. The longer lifetime of the charge carriers in heterostructure-based devices effectively suppresses the charge carrier recombination process.[29] ZTO-based devices also have a shorter lifetime compared with other devices. As a result, carrier density has decreased, and recombination resistance has been reduced at the interface between the photoanode and the electrolyte.[27] However, decreasing interface resistance is one of the effective techniques to enhance the charge transfer process and avoid the recombinational process.[27] It was primarily based on minimizing the charge carrier trap, and this trap is responsible for reducing perovskite efficiency. Thus, the obtained J–V curves and EIS measurements provide many hints for further improving the efficiency of the PSC device.

4.4. Stability analysis

Fig. 9 shows the stability analysis of the pristine ZTO and hybrid ZTO–ZnO, ZTO–SnO₂ composite-based PSC devices. The ISOS-L-1 standard protocol was followed to explore the stability of the devices. The devices were illuminated with a lamp irradiated at 100 mW cm^{-2}, at an ambient temperature and humidity of 24 ± 4 °C and 45 ± 5%, respectively.[35] We measured the photovoltaic performance of the fabricated devices periodically and kept them under continuous illumination at all times. All the fabricated PSC devices decreased stability in the presence of light, similar to the observations of Huang et al.[73]

Under continuous lamp illumination, we observed significant decreases in the PSC devices' photovoltaic performance (Fig. 9(a)–(d)). Pristine ZTO-based PCE devices diminished with time due to decreased J_{sc} and FF levels. In the case of ZTO–ZnO and ZTO–SnO₂ heterostructure-based PSC devices, a relatively low degradation was observed compared to the pristine ZTO-based device. Also, the electrode materials have not deteriorated strongly with time, as the V_{oc} appeared to show low degradation.[74] Degradation of the active layer and the device constituents was the primary cause of performance degradation. A reduction in J_{sc} and FF can be attributed to the photodegradation of perovskites. Photodegradation of organo-metal halide
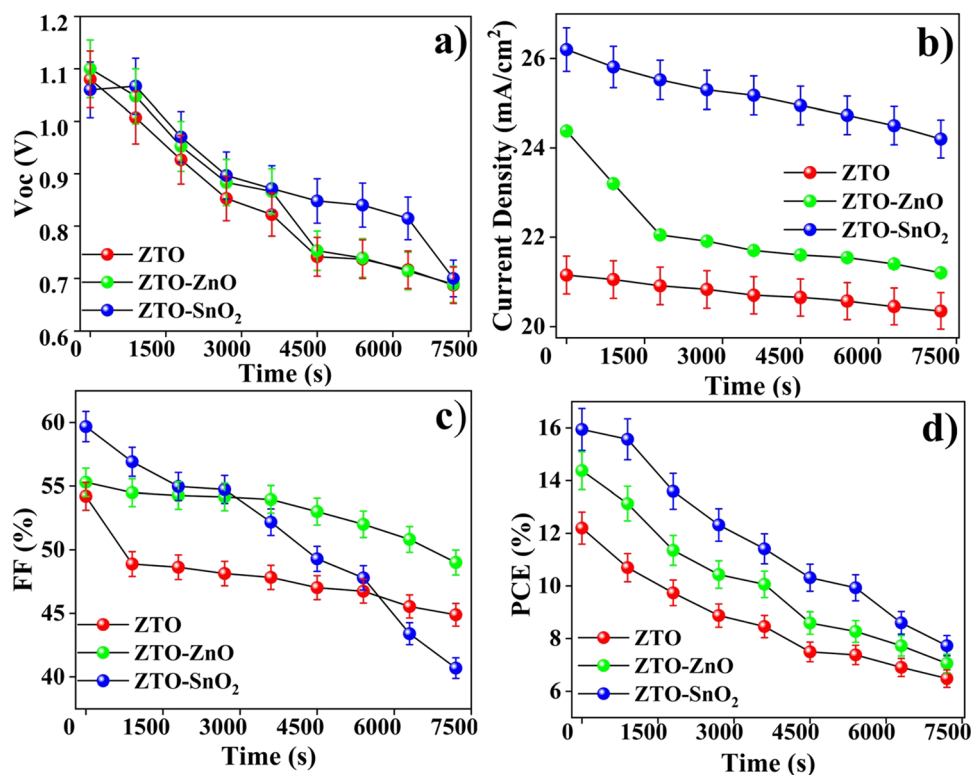

Fig. 9 (a) Stability egging test for the pristine ZTO, and composite ZTO–ZnO, ZTO–SnO₂ heterostructure-based PSC devices; open-circuit voltage, (b) short circuit current, (c) fill factor, and (d) power conversion efficiency.
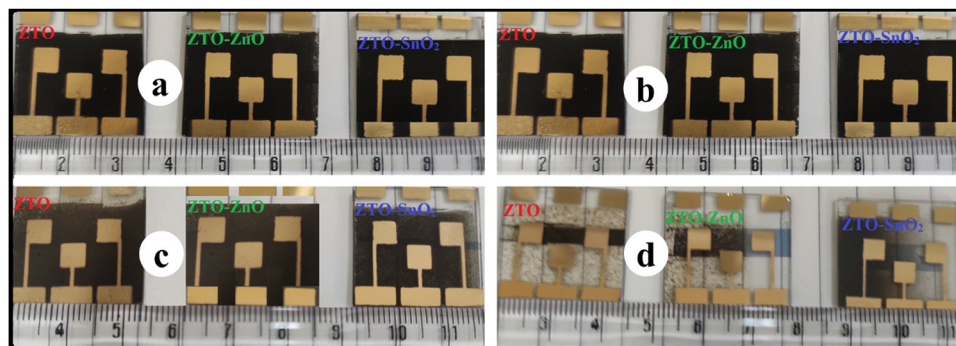

Fig. 10 Visible degradation of the pristine ZTO, and composite ZTO–ZnO, ZTO–SnO₂ heterostructure-based PSC devices; (a) as-fabricated, (b) after 10 days, (c) after 20 days, and (d) after 30 days.

perovskite semiconductors is observed, although the degradation rate varies with the intensity of the incident light.[29] Decomposition of perovskites into constituents results in the loss of optical and electrical properties.[29,35]

These results suggest that the photoanode side is relatively stable under white LED lamp illumination. In the long run, the decline in V_{oc} and FF overtook the increase in J_{sc}, reducing PCE. Fig. 10 shows the visible degradation of the fabricated PSC devices. The photographs were taken following fabrication at 10, 20, and 30 day time intervals. It is identified that the fabricated PSC devices have a maximum lifetime of less than a month. However, making an encapsulation layer on top of devices can aid in improving the lifetime of the devices to some extent. Thus, the obtained stability results indicate the potential application of ZTO–ZnO and ZTO–SnO$_2$ heterostructures as ETL materials for PSC device fabrication and a further improvement in the device performance.

5. Conclusion

Pristine ZTO, composite ZTO–ZnO, and ZTO–SnO$_2$ heterostructure systems were prepared by a simple solid-state calcination technique and employed as ETLs for PSC devices. The HR-TEM analysis confirms the crystallinity and its dependence on the stoichiometric ratio of the precursors. Synthesized samples exhibited a polyhedron surface morphology, which significantly impacts the change transport process of the PSC devices. The suitable surface work function of an ETL can facilitate effective charge carrier injection/collection, as well as control the recombination process. Perovskite solar cells fabricated using composite ZTO–ZnO and ZTO–SnO$_2$ electron transport layers exhibited enhanced power conversion efficiency due to the multiband charge transport mechanism compared to the ZTO-based devices. Moreover, the PSC device based on ZTO–SnO$_2$ exhibited a maximum efficiency of 15.9%, whereas ZTO–ZnO exhibited a maximum efficiency of 14.3%, which is relatively higher than the 12.6% for pristine ZTO. Hence, the results suggest that the ZTO–SnO$_2$ heterostructure can be a potential ETL material for constructing stable PSC devices.

Conflicts of interest

The authors declare that they have no conflict of interests or personal relationships that could have appeared to influence the work reported in this paper.

Acknowledgements

References

1 IRENA, *World Energy Transitions Outlook: 1.5 °C Pathway*, 2021.

2 J. Zhang, *ES Energy Environ.*, 2021, **14**, 1–2.

3 X. Jiang, Y. Chen, X. Meng, W. Cao, C. Liu, Q. Huang, N. Naik, V. Murugadoss, M. Huang and Z. Guo, *Carbon*, 2022, **191**, 448–470.

4 G. Yuan, T. Wan, A. BaQais, Y. Mu, D. Cui, M. A. Amin, X. Li, B. Bin Xu, X. Zhu, H. Algadi, H. Li, P. Wasnik, N. Lu, Z. Guo, H. Wei and B. Cheng, *Carbon*, 2023, **212**, 1–9.

5 B. S. Boshoman, F. O. Fatoba and J. T. Jen, *Eng. Sci.*, 2023, 1–14.

6 J. Wang, R. Fu, S. Wen, P. Ning, M. H. Helal, M. A. Salem, B. Bin Xu, Z. M. El-Bahy, M. Huang, Z. Guo, L. Huang and Q. Wang, *Progress and current challenges for CO$_2$ capture materials from ambient air,* Springer International Publishing, 2022, vol. 5.

7 T. Webb, S. J. Sweeney and W. Zhang, *Adv. Funct. Mater.*, 2021, 31.

8 G. de, M. Jannuzzi and C. A. de Melo, *Energy Sustainable Dev.*, 2013, **17**, 40–46.

9 C. Li, M. Feng, F. Guo, Q. Jiang, N. Li, Z. Guo and X. Liu1, *Eng. Sci.*, 2022, **19**, 1–4.

10 P. Zhang, S. Wu, Y. Chen, X. Li, F. Sun, M. Liu, Z. Chen and S. Li, *Eng. Sci.*, 2022, **20**, 180–187.

11 N. G. Park, *Nat. Sustainability*, 2021, **4**, 192–193.

12 H. Min, D. Y. Lee, J. Kim, G. Kim, K. S. Lee, J. Kim, M. J. Paik, Y. K. Kim, K. S. Kim, M. G. Kim, T. J. Shin and S. I. Seok, *Nature*, 2021, **598**, 444–450.

13 A. Harter, S. Mariotti, L. Korte, R. Schlatmann, S. Albrecht and B. Stannowski, *Prog. Photovoltaics*, 2023, 1–11.

14 J. W. Lee, T. Y. Lee, P. J. Yoo, M. Grätzel, S. Mhaisalkar and N. G. Park, *J. Mater. Chem. A*, 2014, **2**, 9251–9259.

15 J. Y. Kim, J. W. Lee, H. S. Jung, H. Shin and N. G. Park, *Chem. Rev.*, 2020, **120**, 7867–7918.

16 M. A. Haque, A. D. Sheikh, X. Guan and T. Wu, *Adv. Energy Mater.*, 2017, 7, 1–23.

17 J. Chen and N. G. Park, *ACS Energy Lett.*, 2020, **5**, 2742–2786.

18 Y. Liu, M. Bag, L. A. Renna, Z. A. Page, P. Kim, T. Emrick, D. Venkataraman and T. P. Russell, *Adv. Energy Mater.*, 2016, **6**, 1–7.

19 J. Burschka, N. Pellet, S. J. Moon, R. Humphry-Baker, P. Gao, M. K. Nazeeruddin and M. Grätzel, *Nature*, 2013, **499**, 316–319.

20 S. N. A. Shah, Z. Shah, M. Hussain and M. Khan, *Bioinorg. Chem. Appl.*, 2017, 1–12.

21 J. Kim, G. Kim, T. K. Kim, S. Kwon, H. Back, J. Lee, S. H. Lee, H. Kang and K. Lee, *J. Mater. Chem. A*, 2014, **2**, 17291–17296.

22 P. Wu, S. Wang, X. Li and F. Zhang, *J. Mater. Chem. A*, 2021, **9**, 19554–19588.

23 F. Ali, N. D. Pham, L. Fan, V. Tiong, K. Ostrikov, J. M. Bell, H. Wang and T. Tesfamichael, *ACS Appl. Energy Mater.*, 2019, **2**, 5456–5464.

24 K. Jung, J. Lee, C. Im, J. Do, J. Kim, W. S. Chae and M. J. Lee, *ACS Energy Lett.*, 2018, **3**, 2410–2417.

25 M. Neophytou, M. De Bastiani, N. Gasparini, E. Aydin, E. Ugur, A. Seitkhan, F. Moruzzi, Y. Choaie, A. J. Ramadan, J. R. Troughton, R. Hallani, A. Savva, L. Tsetseris, S. Inal, D. Baran, F. Laquai, T. D. Anthopoulos, H. J. Snaith, S. De Wolf and I. McCulloch, *ACS Appl. Energy Mater.*, 2019, **2**(11), 8090–8097.

26 A. Bera, A. D. Sheikh, M. A. Haque, R. Bose, E. Alarousu, O. F. Mohammed and T. Wu, *ACS Appl. Mater. Interfaces*, 2015, **7**, 12404–12411.

27 M. Abuhelaiqa, N. Shibayama, X. X. Gao, H. Kanda and M. K. Nazeeruddin, *ACS Appl. Energy Mater.*, 2021, **4**, 3424–3430.

28 X. Xu, H. Zhang, J. Shi, J. Dong, Y. Luo, D. Li and Q. Meng, *J. Mater. Chem. A*, 2015, **3**, 19288–19293.

29 H. Guo, H. Zhang, J. Yang, H. Chen, Y. Li, L. Wang and X. Niu, *ACS Appl. Energy Mater.*, 2018, **1**, 6936–6944.

30 S. S. Mali, C. S. Shim, H. Kim and C. K. Hong, *J. Mater. Chem. A*, 2016, **4**, 12158–12169.

31 H. J. Snaith, A. Abate, J. M. Ball, G. E. Eperon, T. Leijtens, N. K. Noel, S. D. Stranks, J. T. W. Wang, K. Wojciechowski and W. Zhang, *J. Phys. Chem. Lett.*, 2014, **5**, 1511–1515.

32 R. Liu, W. Du, Q. Chen, F. Gao, C. Wei, J. Sun and Q. Lu, *RSC Adv.*, 2013, **3**, 2893–2896.

33 M. Liu, H. Wu, Y. Wu, P. Xie, R. A. Pashameah, H. M. Abo-Dief, S. M. El-Bahy, Y. Wei, G. Li, W. Li, G. Liang, C. Liu, K. Sun and R. Fan, *Adv. Compos. Hybrid Mater.*, 2022, **5**, 2021–2030.

34 R. Ramanathan, M. Zinigrad, D. Kasinathan and R. K. Poobalan, *ACS Appl. Energy Mater.*, 2022, **5**, 11506–11516.

35 A. K. Chauhan and P. Kumar, *J. Mater. Sci.: Mater. Electron.*, 2019, **30**, 9582–9592.

36 Y. Shao, Y. Fang, T. Li, Q. Wang, Q. Dong, Y. Deng, Y. Yuan, H. Wei, M. Wang, A. Gruverman, J. Shield and J. Huang, *Energy Environ. Sci.*, 2016, **9**, 1752–1759.

37 S. Das and V. Jayaraman, *Prog. Mater. Sci.*, 2014, **66**, 112–255.

38 L.-B. Li, Y.-F. Wang, H.-S. Rao, W.-Q. Wu, K.-N. Li, C.-Y. Su and D.-B. Kuang, *ACS Appl. Mater. Interfaces*, 2013, **5**, 11865–11871.

39 E. Samuel, T. G. Kim, C. W. Park, B. Joshi, M. T. Swihart and S. S. Yoon, *ACS Sustainable Chem. Eng.*, 2019, **7**, 14031–14040.

40 N. G. Park and H. Segawa, *ACS Photonics*, 2018, **5**, 2970–2977.

41 D. Wang, C. Wu, W. Luo, X. Guo, B. Qu, L. Xiao and Z. Chen, *ACS Appl. Energy Mater.*, 2018, **1**, 2215–2221.

42 B. Roose, C. M. Johansen, K. Dupraz, T. Jaouen, P. Aebi, U. Steiner and A. Abate, *J. Mater. Chem. A*, 2018, **6**, 1850–1857.

43 F. Sadegh, S. Akin, M. Moghadam, V. Mirkhani, M. A. Ruiz-Preciado, Z. Wang, M. M. Tavakoli, M. Graetzel, A. Hagfeldt and W. Tress, *Nano Energy*, 2020, **75**, 105038.

44 G. Martínez-Denegri, S. Colodrero, M. Kramarenko and J. Martorell, *ACS Appl. Energy Mater.*, 2018, **1**, 5548–5556.

45 Y. Li, F. Yang, Y. Wang, G. Shi, Y. M. Maung, J. Yuan, S. Huang and W. Ma, *Sol. RRL*, 2020, **4**, 1–8.

46 Y. C. Liang and Y. Chao, *RSC Adv.*, 2019, **9**, 6482–6493.

47 X. Gong, T. Wang, G. Yin, Q. Peng, Y. Chen, X. Wang, X. Qi, Y. Jiang, Z. Liu, Y. Shen and M. Wang, *J. Mater. Chem. A*, 2021, **9**, 25567–25575.

48 W. Wang, Z. Zhang, Y. Cai, J. Chen, J. Wang, R. Huang, X. Lu, X. Gao, L. Shui, S. Wu and J. M. Liu, *Nanoscale Res. Lett.*, 2016, **11**, 316.

49 Z. Liu, B. Sun, X. Liu, J. Han, H. Ye, Y. Tu, C. Chen, T. Shi, Z. Tang and G. Liao, *J. Mater. Chem. A*, 2018, **6**, 7409–7419.

50 W. Melitz, J. Shen, A. C. Kummel and S. Lee, *Surf. Sci. Rep.*, 2011, **66**, 1–27.

51 S. C. Dixon, D. O. Scanlon, C. J. Carmalt and I. P. Parkin, *J. Mater. Chem. C*, 2016, **4**, 6946–6961.

52 A. Klein, C. Körber, A. Wachau, F. Säuberlich, Y. Gassenbauer, R. Schafranek, S. P. Harvey and T. O. Mason, *Thin Solid Films*, 2009, **518**, 1197–1203.

53 C. Liu, A. Piyadasa, M. Piech, S. Dardona, Z. Ren and P. X. Gao, *J. Mater. Chem. C*, 2016, **4**, 6176–6184.

54 R. Ramarajan, M. Kovendhan, K. Thangaraju, D. P. Joseph and R. R. Babu, *Appl. Surf. Sci.*, 2019, **487**, 1385–1393.

55 R. Jaramillo and S. Ramanathan, *Adv. Funct. Mater.*, 2011, **21**, 4068–4072.

56 C. Zhang, W. Luan and Y. Yin, *Energy Procedia*, 2017, **105**, 793–798.

57 M. G. Helander, M. T. Greiner, Z. B. Wang, W. M. Tang and Z. H. Lu, *J. Vac. Sci. Technol., A*, 2011, **29**, 011019.

58 P. P. Das and P. Sujatha Devi, *Inorg. Chem.*, 2014, **53**, 10797–10799.

59 S. S. Mali, C. S. Shim and C. K. Hong, *Sci. Rep.*, 2015, **5**, 1–14.

60 D. Gültekin and H. Akbulut, *Acta Phys. Pol., A*, 2016, **129**, 803–805.

61 D. Lan, *Prog. Photovoltaics*, 2020, **28**, 533–537.

62 A. Agresti, A. Pazniak, S. Pescetelli, A. Di Vito, D. Rossi, A. Pecchia, M. Auf der Maur, A. Liedl, R. Larciprete, D. V. Kuznetsov, D. Saranin and A. Di Carlo, *Nat. Mater.*, 2019, **18**, 1228–1234.

63 R. Chen, J. Cao, Y. Duan, Y. Hui, T. T. Chuong, D. Ou, F. Han, F. Cheng, X. Huang, B. Wu and N. Zheng, *J. Am. Chem. Soc.*, 2019, **141**, 541–547.

64 F. Wang, Y. Zhang, M. Yang, J. Du, L. Xue, L. Yang, L. Fan, Y. Sui, J. Yang and X. Zhang, *Nano Energy*, 2019, **63**, 1–8.

65 F. Mohamadkhani, S. Javadpour and N. Taghavinia, *Sol. Energy*, 2019, **191**, 647–653.

66 R. Tui, H. Sui, J. Mao, X. Sun, H. Chen, Y. Duan, P. Yang, Q. Tang and B. He, *J. Colloid Interface Sci.*, 2023, **640**, 918–927.

67 M. Kohan, T. Mahmoudi, Y. Wang, Y. H. Im and Y. B. Hahn, *Appl. Surf. Sci.*, 2023, **613**, 156068.

68 A. K. Jena, A. Kulkarni and T. Miyasaka, *Chem. Rev.*, 2019, **119**, 3036–3103.

69 D. Y. Son, K. H. Bae, H. S. Kim and N. G. Park, *J. Phys. Chem. C*, 2015, **119**, 10321–10328.

70 A. Todinova, L. Contreras-Bernal, M. Salado, S. Ahmad, N. Morillo, J. Idígoras and J. J. A. Anta, *ChemElectroChem*, 2017, **4**, 2891–2901.

71 B. R. Bade, K. B. Kore, S. R. Rondiya, D. S. Nilegave, M. P. Nasane, S. B. Jathar, S. V. Barma, S. R. Jadkar and A. M. Funde, *ES Energy Environ.*, 2021, **13**, 31–36.

72 M. Spalla, E. Planes, L. Perrin, M. Matheron, S. Berson and L. Flandin, *ACS Appl. Energy Mater.*, 2019, **2**, 7183–7195.

73 H. Huang, J. Shi, L. Zhu, D. Li, Y. Luo and Q. Meng, *Nano Energy*, 2016, **27**, 352–358.

74 S. B. Jathar, S. R. Rondiya, B. R. Bade, M. P. Nasane, S. V. Barma, Y. A. Jadhav, A. V. Rokade, K. B. Kore, D. S. Nilegave, P. U. Tandale, S. R. Jadkar and A. M. Funde, *ES Mater. Manuf.*, 2021, **12**, 72–77.